npj | climate and atmospheric science

Article

Published in partnership with CECCR at King Abdulaziz University

https://doi.org/10.1038/s41612-025-01256-w

Observational evidence of reduced Bay of Bengal lightning since 2020 linked to cloud responses to shipping emission regulations

Qinjian Jin[1] ✉, Jianping Huang[2], Jiangfeng Wei[3] & Bing Pu[1] ✉

Lightning plays a crucial role in the Earth's biogeochemical cycle. Frequent lightning activity over the Bay of Bengal (BoB) has been attributed to shipping emissions through aerosol–cloud interactions in modeling studies but lacks observational confirmation. Here, we present observational evidence linking frequent lightning to the response of deep clouds to ship-emitted sulfate aerosols. These aerosols cause higher cloud tops in mid-to-high clouds, smaller cloud droplet sizes at the bases of low clouds, and increased ice water content with smaller ice particles in deep clouds along shipping lanes, resulting in more lightning strikes than in surrounding areas. The 2020 fuel regulation, which reduced SO_2 emissions by 66% over the BoB, led to lower cloud tops, reduced ice water content, larger cloud droplets, and consequently an 11% decline in lightning frequency during the period of 2020–2023 relative to its climatology. Our findings indicate that shipping emissions contribute at least 17% to the lightning frequency in the BoB region. This study provides observational evidence that changes in shipping emissions—particularly those driven by recent regulations—can significantly influence lightning frequency by altering the microphysical properties of deep clouds. It underscores the broader atmospheric impact of maritime policies, extending beyond local radiative effects to influence convective processes and natural hazards.

Atmospheric aerosols have a profound effect on Earth's radiation budget, influencing both regional and global climate. They interact with solar and terrestrial radiation directly by scattering and absorbing radiation[1] and indirectly by perturbing cloud micro- and macro-physical properties, such as cloud condensation nuclei (CCN) and ice nucleating particles (INP)[2]. Among various aerosol species, sulfate aerosols have the strongest cooling effect on the climate system; however, current estimates of this effect remain highly uncertain[3]. Human-emitted sulfur dioxide (SO_2) is a key source of sulfate aerosols, and its global emissions have significantly decreased over the past several decades due to the implementation of air quality regulations, such as the Clean Air Act in the U.S.[4]. This reduction in SO_2 emissions may contribute to the recent acceleration of global warming[5–8].

Although accounting for only ~10% of global total anthropogenic SO_2 emissions[9], international shipping emissions play a critical role in the formation and development of marine clouds through aerosol–cloud interactions, largely owing to the low background concentration of sulfate aerosols from natural sources over the open ocean. Ship-emitted SO_2 can affect shallow clouds over the Pacific and Atlantic Oceans and deep clouds in strong convection systems[10]. The "anomalous cloud lines", i.e., long strings of bright low-marine clouds around ship exhaust, were first observed in 1965 by satellite and later known as ship tracks[11]. Since then, numerous studies have investigated the formation mechanism of ship tracks through both observations and numerical simulations. It is found that sulfate aerosols from shipping emissions act as CCN and promote the formation of marine low clouds[12–15]. On the other hand, the impacts of ship-emitted sulfate aerosols on deep clouds are reflected by the enhanced lightning frequency over two major shipping lanes in the Bay of Bengal (BoB) and South China Sea compared to its surrounding regions [e.g., ref. 16], as shown in Fig. 1. Nevertheless, the mechanisms of the enhanced lightning remain

[1]Department of Geography and Atmospheric Science, University of Kansas, Lawrence, Kansas, USA. [2]Collaborative Innovation Center for Western Ecological Safety, Lanzhou University, Lanzhou, China. [3]School of Atmospheric Sciences, Nanjing University of Information Science and Technology, Nanjing, China. ✉e-mail: jqj@ku.edu; bpu@ku.edu

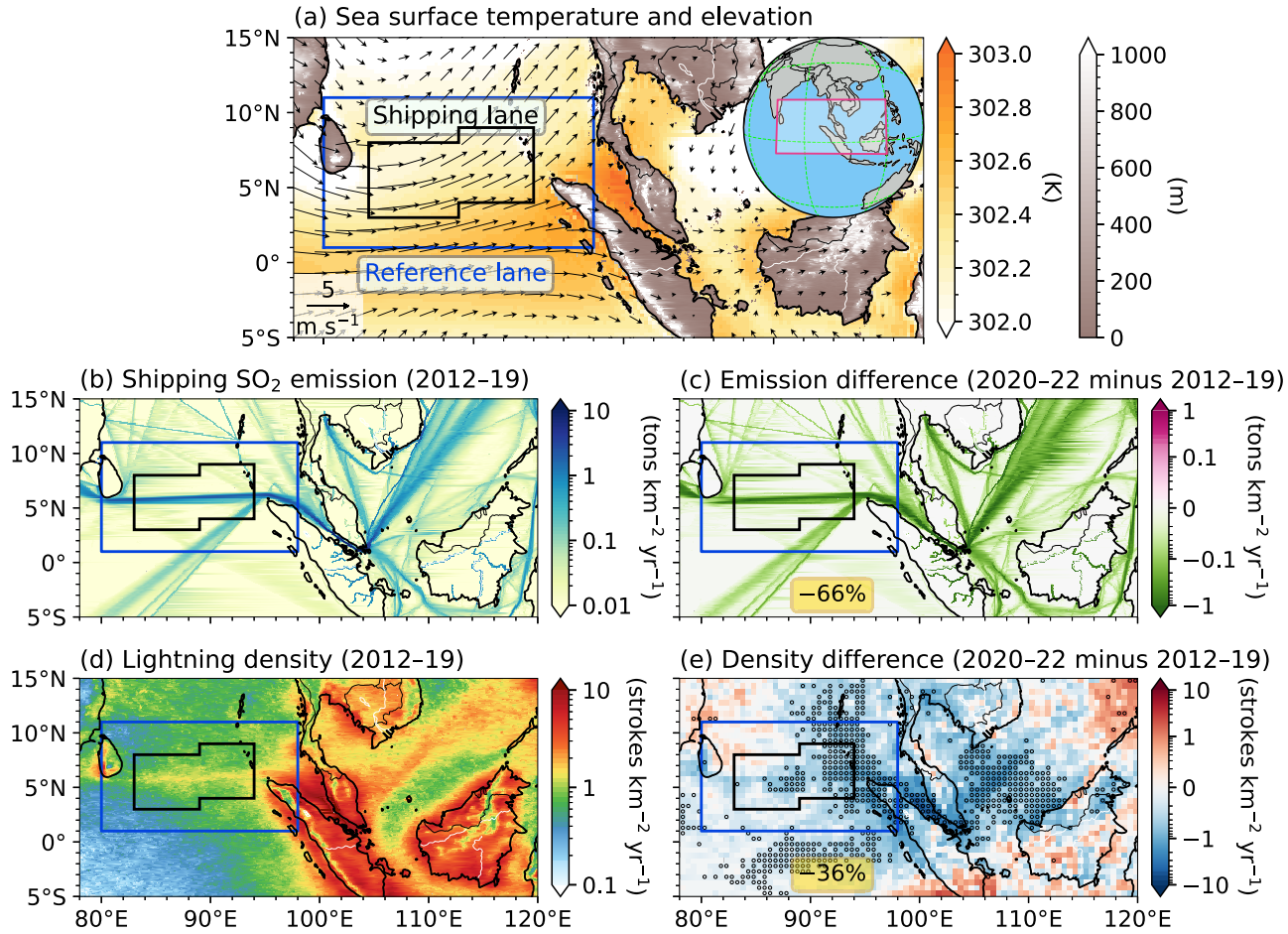

Fig. 1 | Climatology and changes of SO_2 emissions and lightning density. **a** Topography (m) and climatology (2012–2022) of sea surface temperature (SST; K) and circulations (m s^{-1}) at 850 hPa. **b**, **d** SO_2 emission rate (tons km^{-2} yr^{-1}) from international shipping and lightning density (strokes km^{-2} yr^{-1}) averaged over 2012–2019. **c**, **e** Differences in SO_2 emission rates and lightning density during 2020–2022 vs. 2012–2019. The percents in panels (**c**) and (**e**) indicate the area-averaged changes of SO2 emissions and lightning density within the shipping lane (i.e., black polygon). Circles in panel **e** indicate grid cells with statistically significant differences at 95% confidence level. The SST and circulation data are from ERA5; SO_2 emission and lightning data are from CEDS and WWLLN. The blue box represents the domain of interest. The grid cells enclosed by the black polygon are defined as the shipping lane and the remaining grid cells within the blue box are defined as the reference lane. The red box in the inset map shows the location of the study domain over the Bay of Bengal. For more details, please refer to the Methods section. The figure was created using Matplotlib Python package.

disputed despite extensive research efforts, mainly due to a lack of robust observational evidence of aerosol-induced changes in cloud microphysical properties. Modeling studies hypothesize that shipping aerosols enhance deep convection (i.e., strengthening updraft, increasing convective cloud top height, and causing larger ice particles) and thus storm electrification in the shipping lanes[16–19], but observational studies based on the close relationship between the locations of ship transponder events and lightning strokes suggest that tall ships extending up into a high electric field environment could facilitate lightning discharges and thus enhance lightning activity, namely the direct ship interactions[20].

In January 2020, the International Maritime Organization (IMO) imposed a new regulation to reduce sulfur emissions from ships. The new regulation (hereafter IMO 2020) mandates a maximum sulfur mass content of 0.5% (versus 3.5% previously) in marine fuel globally. Consequently, global SO_2 emissions from international shipping decreased from 10.4 Tg in 2019 to 3.0 Tg in 2020 (i.e., a 71% reduction)[21]. This new regulation provides a unique opportunity to study the influences of shipping emissions on cloud formation and lightning intensification in observations. A satellite-based study has already found a reduction of 50% in ship tracks since 2020 compared to the climatological mean over the North Pacific and North Atlantic Oceans[22]. The decreasing ship tracks and consequently the reduction in cloudiness have generated a positive radiative effect at top of the atmosphere in the order of 0.1 W m^{-2} at the global scale[5,6,23,24] that could contribute to the record-breaking global temperatures in 2023 and 2024[7,8].

However, how deep convective clouds respond to the decrease in sulfur emissions from ships due to IMO 2020 remains an open question. A recent study[25] demonstrated a decline in warm liquid cloud-base drop number along the shipping lane over the BoB during the period of 2020–2023 compared to 2010–2019, which may be partially responsible for a 40% drop in lightning density. Although lightning is a complicated process and a significant knowledge gap still exists regarding the exact details of its formation mechanism, it is widely accepted that the occurrence of lightning involves two key processes: separation of electric charge and generation of an electric field above some threshold within a thunderstorm[26,27]. The dominant process of deep convective cloud electrification is the non-inductive charging mechanism where charge separation is achieved through rebounding collisions between larger and denser graupel or hail particles in downdrafts and smaller ice crystals in strong updrafts in the presence of supercooled liquid water[28]. Since graupel and hail particles develop from ice crystals, the latter play a vital role in lightning occurrence—storms that produce large quantities of ice crystals produce lightning with a high chance[29,30]. Ice crystals form through heterogeneous or homogeneous ice nucleation processes, depending on temperature and the availability of INP[31,32]. Both ice nucleation processes require temperatures below freezing and supercooled water, implying that clouds must develop at high altitude.

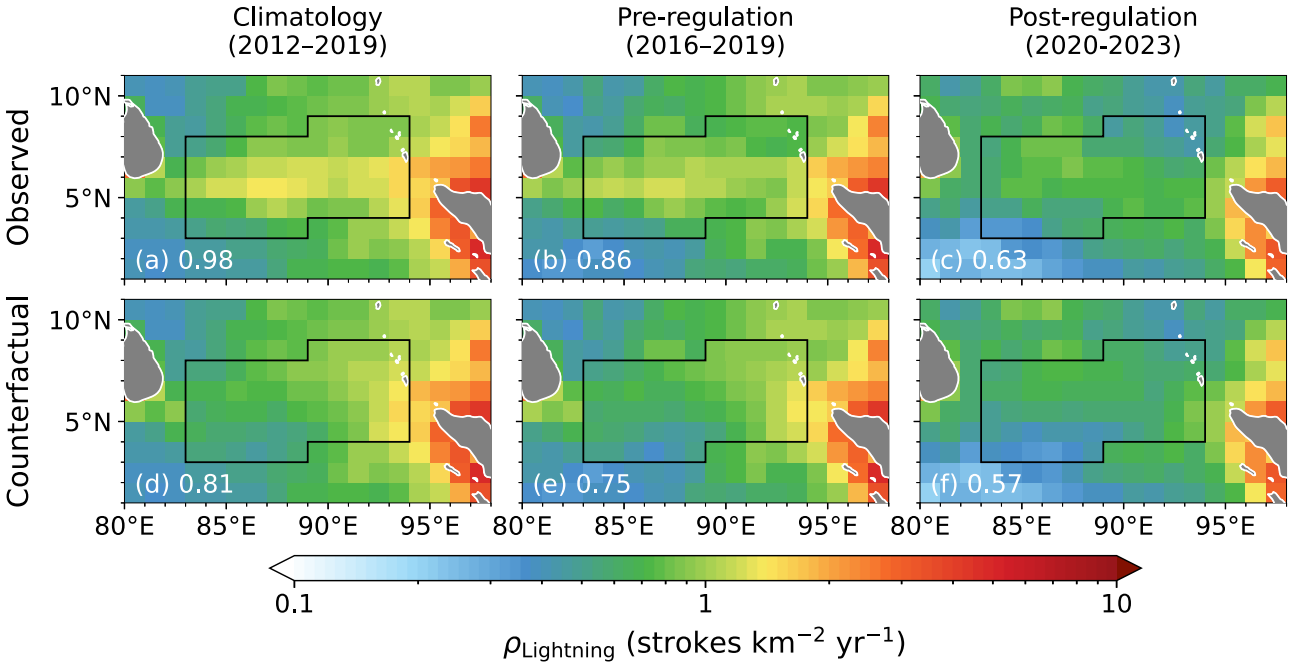

Fig. 2 | Kriging analysis of lightning density. Maps of factual (observed; first row) and counterfactual (second row) values for annual lightning density (strokes km^{-2} yr^{-1}) over the Bay of Bengal for the pre-regulation climatology 2012–2019 (**a**) and (**d**), and the immediate pre-regulation 4-year period 2016–2019 (**b**) and (**e**), and the post-regulation 4-year period 2000–2023 (**c**) and (**f**). The grid cells outlined by black lines are the shipping lane area and the other grid cells are the reference lane area. The number in each panel is the area-averaged lightning density within the shipping lane area. Data are from WWLLN. The figure was created using Matplotlib Python package.

Therefore, examining changes in deep cloud properties, such as cloud top height, sizes of water droplets and ice particles, and ice water path that can influence the formation and abundance of ice crystals and thus graupel and hail, can provide direct and compelling evidence for how changes in shipping emissions influence lightning activity. It is worth mentioning that this study does not aim to investigate the details of charge separation mechanisms; instead, by examining changes in cloud properties that are closely linked to ice crystal formation and abundance, it provides observational evidence that a reduction in ship-emitted SO_2 can decrease lightning activities by modulating ice crystal formation processes.

Specifically, by analyzing cloud properties, especially deep cloud microphysics from multiple satellite products and surface lightning observations, we have proposed a physical mechanism that is responsible for the frequent lightning activity along the major shipping lane over the BoB and further attributed the weakened lightning after 2020 to the IMO 2020. The BoB is selected because the lightning density demonstrates a vivid contrast between the enhanced values along a narrow shipping corridor in the east-west direction versus reduced values surrounding the major shipping lane over the BoB (Fig. 1). The meridional contrast in lightning density makes this region ideal for examining the effects of ship-emitted aerosols. The effects of shipping activity on lightning are quantified by examining the differences between the factual (observed) and counterfactual values of cloud micro- and macro-physical properties. The counterfactual values are estimated using the regression kriging method and represent the values the variables would have if the impacts of shipping emissions were largely removed or minimized, i.e., only the impacts of meteorological factors are considered. The random forest regression model was used and trained at the grid cells over the reference lane where the least shipping impact was expected. The well-trained regression model was then applied within the shipping lane to estimate the counterfactual values of a variable assumed to be unaffected by the shipping impact. For details of the regression kriging method, please refer to the Methods section. Our analyses showed that i) shipping emissions are linked to higher mid-to-high cloud tops, smaller radius of low cloud droplets, smaller cloud ice particles (4–20 km), and greater ice water path, which promotes the formation of strong convection and thus lightning; ii) the impacts of shipping emissions on cloud properties have been significantly reduced since the implementation of the IMO 2020; and iii) the IMO2020 weakened the lightning activity over the BoB by at least 11% after 2020 and shipping emissions contributed at least 17% to climatological lightning activity over the BoB. Our results provide multiple observational evidence that ship emissions significantly strengthened lightning activity and were responsible for the weakened lightning over the BoB after 2020, underscoring the important impacts of human activity on cloud properties and natural hazards.

Results

Enhanced lightning resulted from shipping emissions and their reduction after IMO 2020

Enhanced lightning activities over the major shipping lane with reference to its surrounding regions over the BoB are detected in the recent decade. Here, the lightning activity is characterized by lightning density, which is defined as the number of lightning strokes per unit area over a specified period. Annual lightning density is calculated with units of strokes km^{-2} $year^{-1}$. Figure 2a–c demonstrates the observed lightning densities for three periods: 2012–2019 (climatology), 2016–2019 immediately before the IMO 2020 regulation (pre-regulation), and 2020–2023 immediately after the regulation (post-regulation). The enhanced lightning density was observed in an east-west-oriented area along the major shipping lanes over the BoB (black box in Fig. 2a) from 2012 to 2019. Along the shipping lanes, a maximum lightning density of ~2 strokes km^{-2} $year^{-1}$ was observed in latitudes from 5°N to 6°N. During the pre-regulation period of 2016–2019, although the enhanced lightning densities were obvious along the shipping lane, the magnitudes were close to the climatological level: with an area-average value of 0.86 for 2016–2019 vs. 0.98 strokes km^{-2} $year^{-1}$ for the climatology. However, during the post-regulation period of 2020–2023, the lightning densities within the shipping lane area decreased to 0.63 strokes km^{-2} $year^{-1}$ (i.e., a 36% decrease from the climatology). The coincidence of reductions in shipping emissions and lightning frequency over BoB after the implementation of IMO 2020 suggests a potential link between the two.

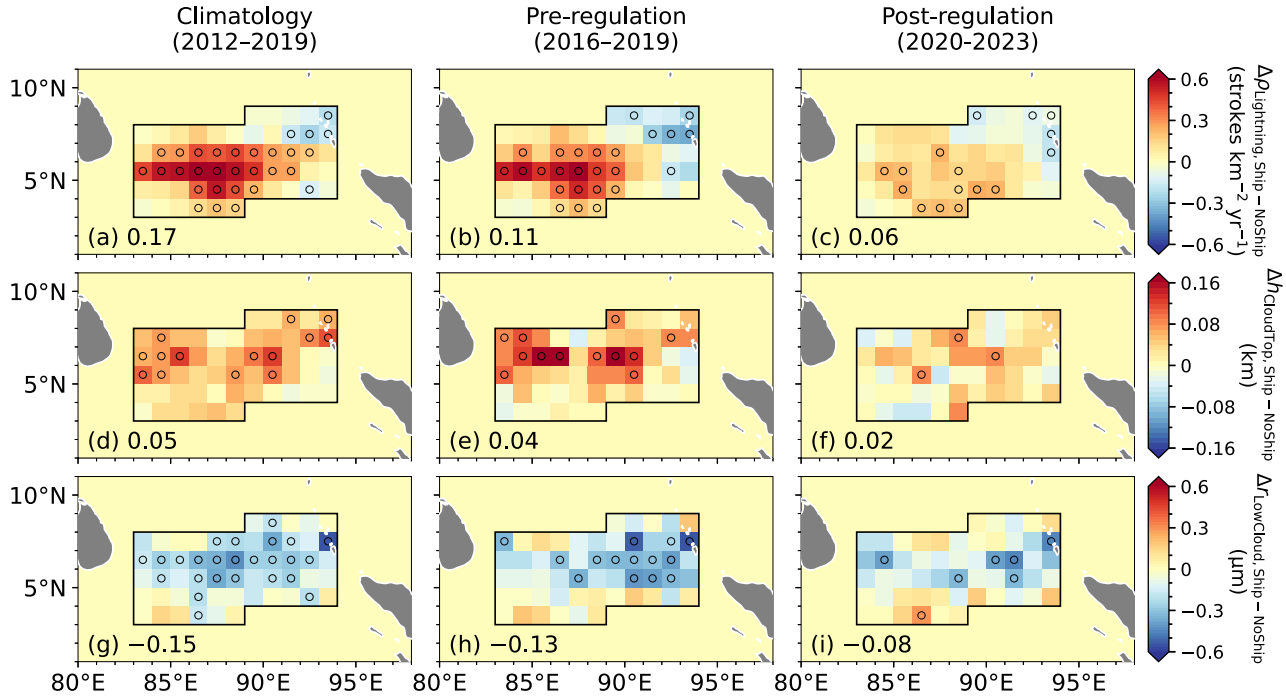

Fig. 3 | Maps of differences between the observed vs. counterfactual values. Observed minus counterfactual differences are shown for **a**–**c** lightning density ρ (strokes km^{-2} yr^{-1}), **d**–**f** height h of mid-to-high cloud top (km), and **g**–**i** radius r (μm) of low cloud droplet. Circles indicate grid cells with statistically significant differences at 95% confidence level. The number in each panel is the area-averaged values within the shipping lane area. Data are from WWLLN and CERES. The figure was created using Matplotlib Python package.

We quantify the effects of shipping emissions on lightning by examining the difference between the factual (observed) and counterfactual values of the lightning density. Figure 2d–f shows that the enhanced lightning density along the major shipping lanes is almost absent in the counterfactual values, implying a significant positive impact of sulfate aerosols emitted from ships on the lightning density. Figure 3a–c shows the differences between the factual vs. counterfactual values of lightning density. Increases in lightning density due to shipping activity are most evident along the major shipping lane around 5.5°N. The area-averaged increases within the shipping lane area are 0.17 (17%), 0.11 (13%), and 0.06 (10%) strokes km^{-2} year^{-1} for the climatology, pre-regulation (2016–2019), and post-regulation (2020–2023), respectively. The increase in lightning activity along the shipping lanes over the BoB in the climatology supports the findings of previous studies [e.g., ref. 17]. In the post-regulation period, the number of grid cells with a statistically significant increase (above the 95% confidence level) in lightning density has decreased to 11 (~50%) vs. 25 and 19 for the climatology and pre-regulation periods, respectively.

To assess how different the shipping perturbed lightning activity and cloud properties (i.e., observed minus counterfactual values) are during the post-regulation period 2020–2023 versus prior 4-year periods (2012–2015 and 2016–2019) and their climatological values, we estimated and compared the probability distribution functions (PDF) of the area-averaged shipping perturbation values within the shipping lane using the Bootstrap method, as shown in Fig. 4a. The PDF for the post-regulation period (2020–2023) is statistically significantly different at the 95% confidence level from that for the climatology (2012–2019): the 95% confidence intervals of the two PDFs have no overlap. This indicates that the IMO 2020 regulation has significantly weakened the lightning activity in the shipping lane area over the BoB. Note that the PDFs for the periods of 2012–2015, 2016–2019, and 2020–2023 demonstrate a shift toward zero difference, but the first two PDFs before the IMO 2020 regulation overlap with the PDF for the climatological period. The above results demonstrate that the IMO 2020 regulation has resulted in a weakened impact of shipping emissions on the lightning density over the BoB.

Response of cloud top height and droplet size to shipping emissions

The physical mechanism of the enhanced lightning density over the shipping lane area and its weakened magnitude after the IMO 2020 regulation can be understood by examining cloud responses to shipping emissions. Two cloud properties are analyzed: the height of the mid-to-high cloud top and the radius of the cloud droplet of low water cloud. The former is closely linked to the strength of deep convection where lightning occurs, and the latter is highly susceptible to aerosol concentrations since i) cloud droplets generally tend to be smaller in environments with higher aerosol concentrations and constant water vapor supply, and ii) the low cloud is usually the place where aerosols enter the clouds and get activated to form CCN and INP. Here, we argue that although low clouds are generally considered to have little contribution to lightning occurrence, in strong convective regions like the BoB, low clouds such as small cumulus clouds can develop into cumulonimbus clouds[33] and thus can be linked to lightning activity.

The observed and counterfactual heights of the mid-to-high cloud top are shown in Supplementary Fig. S1. For the climatology and pre-regulation periods, the observed heights illustrate greater values of up to 9.6 km along the major shipping lane around 6°N than those in the reference lane area. However, the contrast of the heights between the shipping and reference lanes becomes weaker for the post-regulation period of 2020–2023. The differences between the observed and counterfactual heights are 50 and 40 m for the climatology and pre-regulation periods, respectively, which are much greater than the post-regulation value of 20 m, as shown in Fig. 3d–f. These differences have the same order of magnitude as the standard deviation (56 m) of the heights between 2012 and 2023, suggesting that the differences are quite large despite their magnitudes being 2–3 orders smaller than the absolute values of the cloud height. Note that the above analysis of CERES mid-to-high cloud top height bears poorly quantified uncertainty since the uncertainty of CERES cloud top height retrievals varies, depending on cloud types and atmospheric conditions[34]. Moreover, the areas with statistically significant differences are larger in the climatology (14 grid cells) and pre-regulation period (12 grid cells) than in the post-regulation period

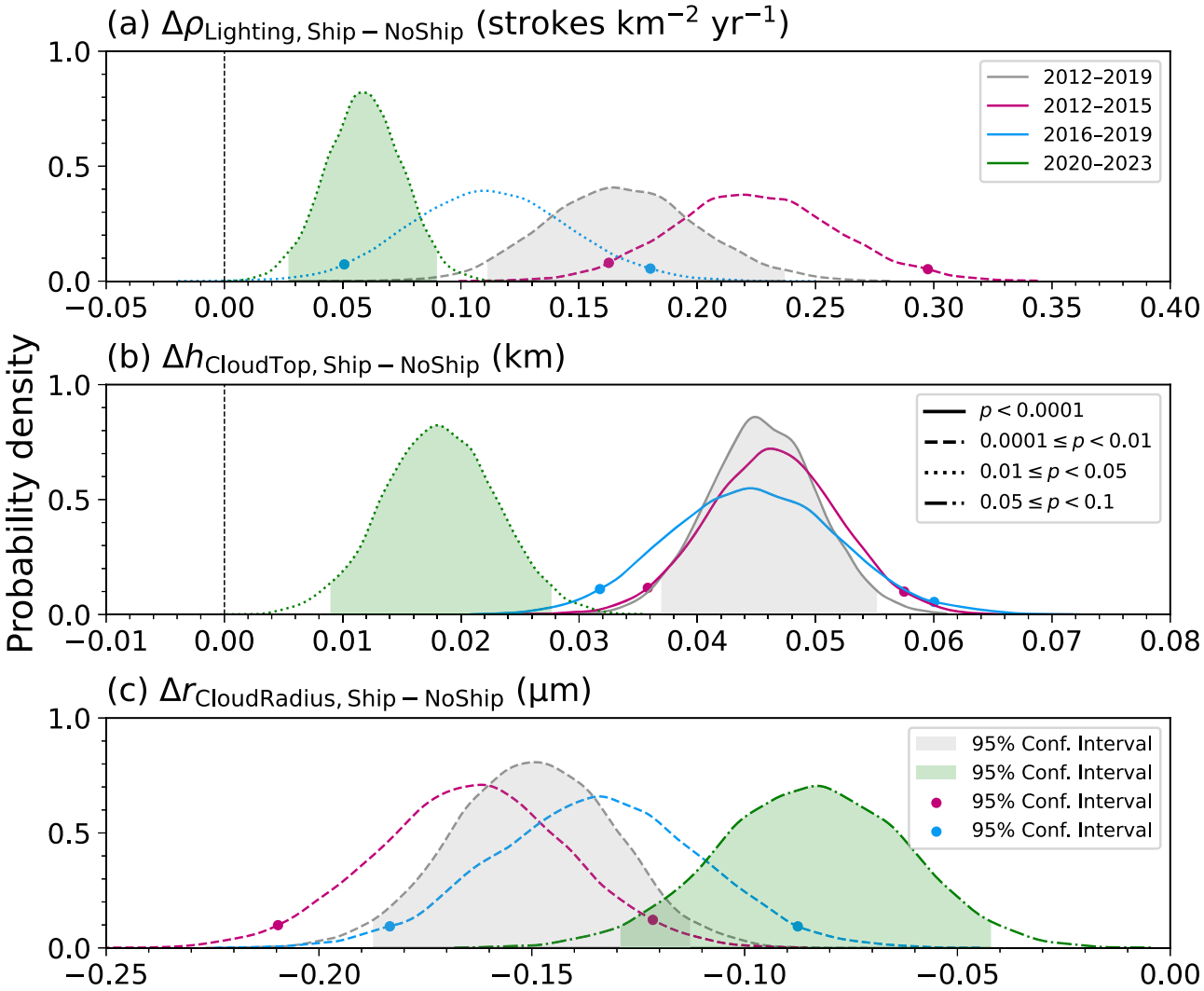

Fig. 4 | Probability density for the Ship minus NoShip difference. The probability densities are estimated over the shipping lane grid cells for the annual **a** lightning density (strokes km^{-2} yr^{-1}), **b** altitude (km) of the mid-to-high cloud top, and **c** radius (μm) of the low cloud droplets. They are calculated through the Gaussian Kernel Density Estimation method. The gray, red, blue, and green curves are the differences for the pre-regulation climatology (2012–2019), 2012–2015, 2016–2019, and 2020–2023, respectively. The solid, dashed, dotted, and dash-dotted lines represent various *p*-values. Shadings and filled circles indicate the 95% confidence intervals of the distributions. The three legends across the three panels are applicable to each of the three panels. The figure was created using Matplotlib Python package.

(3 grid cells). The area-averaged heights within the shipping lane area during the post-regulation period are statistically significantly lower than those during the periods before the IMO 2020 regulation: no overlap between the PDF during the post-regulation vs. the PDFs for other periods, as shown in Fig. 4b. These results indicate that higher mid-to-high cloud top is associated with the enhanced lightning density, and this association has been weakened after the IMO 2020 regulation. The elevated height of the mid-to-high cloud top along the major shipping lane is further verified by the relatively low cloud top temperature and pressure (Supplementary Figs. S2, S3). Further analysis shows that shipping-induced impacts on cloud top temperature and pressure of mid-to-high clouds have been reduced during the post-regulation period (Supplementary Fig. S4). Although CERES retrievals of cloud top properties have considerable uncertainties, the consistent changes in height, temperature, and pressure of the mid-to-high cloud top indicate strong robustness of the above analysis.

The elevated height of the mid-to-high cloud top along the major shipping lane is consistent with previous findings that smaller cloud droplets in polluted regions due to high aerosol concentrations lead to longer cloud lifetime and taller cloud top[35,36]. Supplementary Fig. S5 shows a mean radius as low as 13.5 μm along the major shipping lane around 6°N during all periods vs. a greater mean radius up to 15 μm within the reference lane area. The radius during the post-regulation period has increased compared with that during the pre-regulation period, which is associated with the emission reduction of sulfur oxides from ships after the IMO 2020 regulation. Figure 3g–i shows that the differences of the radius between the observed and counterfactual values are negative and have greater magnitudes of 0.15 and 0.13 μm for the climatological and pre-regulation periods, respectively, than that for the post-regulation period with a value of 0.08 μm. The area with statistically significant negative differences is also larger during the first two periods (24 and 13 grid cells) than during the post-regulation period (6 grid cells). These results suggest that the impacts of shipping emissions on cloud droplet size have been reduced after 2020. The PDFs of the area-averaged radius within the shipping lane during various periods are shown in Fig. 4c. Although the 95% confidence intervals of all PDFs are far from zero, they overlap with each other due to their large variations. The increase in cloud droplet radius of low cloud during the post-regulation period is consistent with the results of a recent study that demonstrates a decrease in cloud droplet number concentrations at warm cloud-base along the shipping lane over the Indian Ocean[25]. The

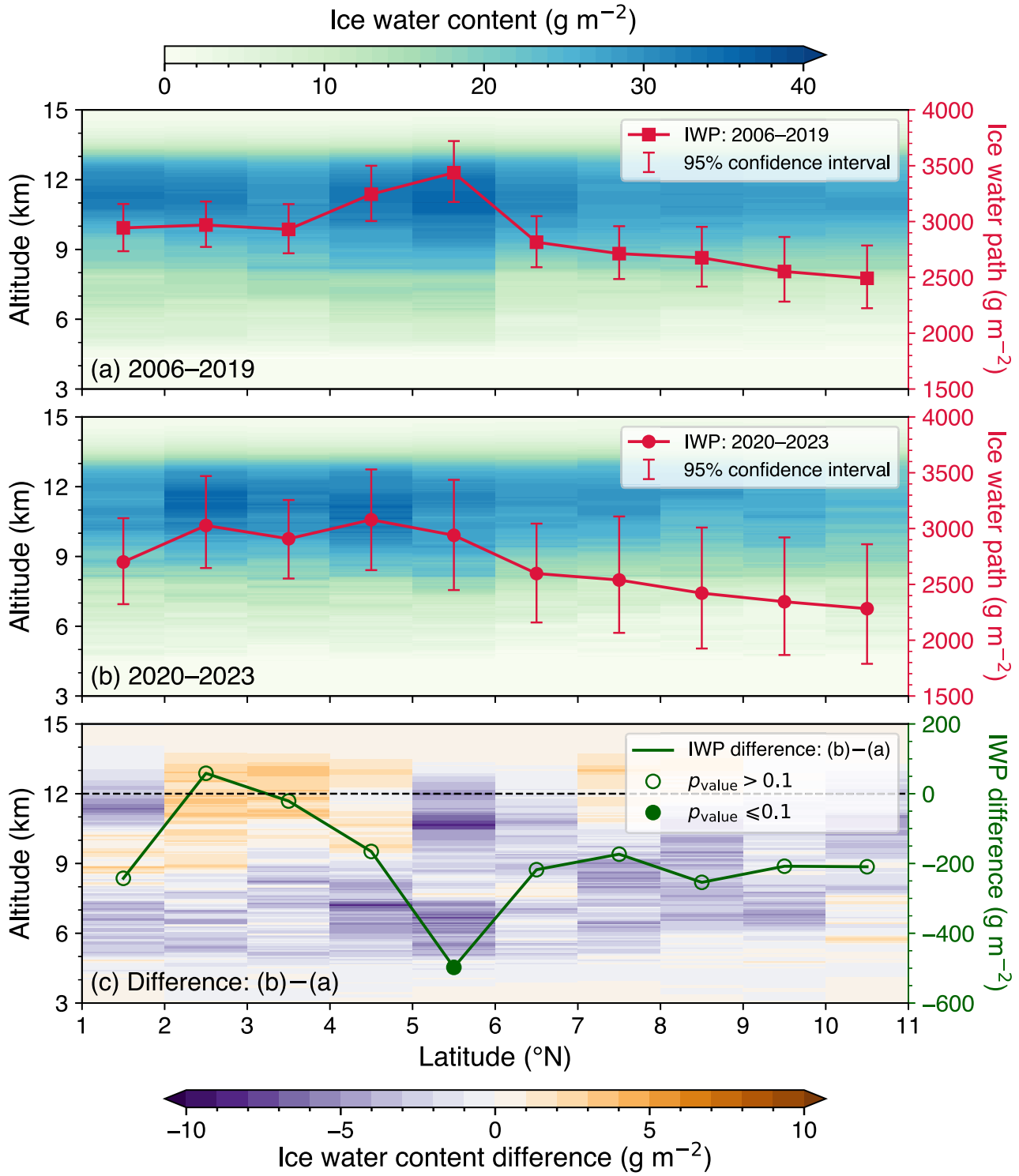

Fig. 5 | Vertical distribution of ice water content. Vertical distribution (shading) and column-integrated (line) values of the zonal (85–90 °E) mean of the meridional annual ice water content (g m^{-2}) for **a** pre-regulation climatology (June 2006–December 2019), **b** post-regulation (January 2020–June 2023), and **c** their difference. Ice water path (IWP) is integrated from 3 to 15 km, beyond which altitude range ice water content is close to zero. Error bars indicate the 95% confidence interval. Open and filled circles in panel (**c**) represent differences with $p > 0.1$ and $p \leq 0.1$, respectively. The bootstrap method was used to estimate the p values. Data are from CALIPSO/CALIOP. The figure was created using Matplotlib Python package.

larger but fewer cloud droplets could enhance the downdraft yet weaken the updraft, which constrains the cloud top to a relatively low altitude and in turn reduces the production of ice crystals and thus graupels, ultimately lowering the chance of rebounding collisions, charge separation, and lightning occurrence in a thunderstorm[37].

Variations in deep cloud properties due to shipping emissions

Since lightning activity is closely associated with deep cloud formation[29,30], the vertical profiles of deep cloud ice properties are further analyzed in this section. The above analyses show that both shipping emissions and lightning density demonstrate strong meridional variations from 1° to 11° N,

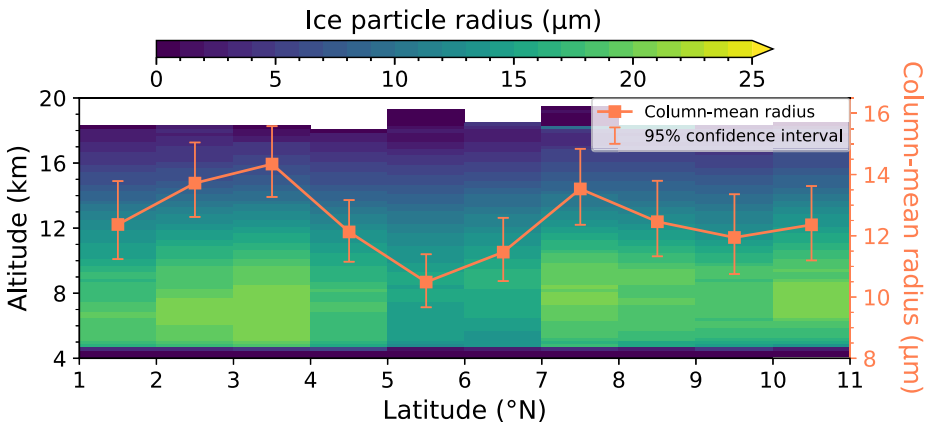

Fig. 6 | Vertical distribution of ice particle radius. Shadings represent the zonal (85–90 °E) mean of meridional ice particle radius (μm) averaged over June 2006–August 2020. Orange curves represent the column-mean (4–20 km) radius with error bars indicating the 95% confidence interval. White color means no data is available. Data are from CloudSat. The figure was created using Matplotlib Python package.

with the peak values at ~5.5°N, so similar meridional variations in deep cloud ice properties are also expected around this latitude. Here, vertical profiles of ice water content and ice particle radius from CALIPSO and CloudSat retrievals, as well as their changes after the IMO 2020 regulation, are examined (Figs. 5 and 6). Elevated ice water content over 20 g m^{-2} was observed between the altitudes of 8 and 13 km (Fig. 5a). As expected, a peak of ice water path integrated between 3 and 15 km was observed at 5.5°N during the period of 2006–2019. However, such a peak disappeared during the post-regulation period of 2020–2023 (Fig. 5b). The changes in the ice water content and ice water path from 2006–2019 to 2020–2023 were dominated by negative values and showed maximum magnitudes at 5.5°N (Fig. 5c). Note that the decrease in ice water path was statistically significant at the 90% confidence level only at 5.5°N with a value of −500 g m^{-2} vs. −200 g m^{-2} at other latitudes, which highlights the impact of shipping emissions on the ice water path.

The higher ice water content along the shipping lane versus in the reference lane is consistent with the meridional variability of the sizes of ice particles. Figure 6. illustrates that the column mean radius is ~13 μm between 4 and 20 km. In the vertical direction, ice particles are larger between 6 and 10 km and generally decrease with altitude above 10 km. In the meridional direction, ice particles are relatively smaller at latitudes from 4.5 to 6.5°N with a minimum radius of 10.5 μm at 5.5°N, which is consistent with the elevated shipping emissions along the shipping lane that tend to result in smaller ice particles. Note that we did not show the difference in ice particle radius before and after the IMO 2020 regulation due to a lack of CloudSat data after August 2020. Our results show that although the ice water path is enhanced along the major shipping lane, the ice particles are smaller than those in the reference lane, implying that the shipping emission-induced increase in ice particle number concentration may have dominated the increase in the ice water path.

Meanwhile, it is worth noting that 1) the meridional ice properties in Figs. 5 and 6 are averaged over the zonal range of 85°E–90°E instead of the full zonal width of the shipping lane because the enhanced lightning densities due to shipping emissions are most obvious in this zonal range (Fig. 1a–c); 2) the 95% confidence intervals of ice water path is larger in the post-regulation period (Fig. 5b) than in the pre-regulation period (Fig. 5a), which is due to a shorter period of observations since 2020 and could reduce the statistical robustness of the changes in ice water path since 2020 (Fig. 5c). We believe that the statistical robustness will be improved when more observations are available; and 3) ice water content retrieved by CALIPSO lidar only represents ice in the very tops of deep convective clouds given the large opacity of such clouds. Thus, Fig. 5 may also indicate another possibility that deep cloud top shifts toward a lower height vs. the changes in the deep cloud microphysics analyzed above. Anyway, both possibilities suggest reduced convection activities and thus less lightning activities due to the reduction in shipping emissions.

Potential impacts of direct ship interactions and meteorological conditions on lightning frequency

The above analyses support the previous hypothesis that the ship-emitted SO_2 can modify the lightning activity over the BoB through the aerosol–cloud interactions, but they do not rule out the potential importance of the direct ship interactions in the lightning enhancement. Ships emit both SO_2 and nitrogen dioxide (NO_2), but no new regulation on NO_2 emissions from ships has been implemented since 2020. Therefore, shipping activities after 2020 can be approximated by the column density of NO_2 remotely sensed from space, as shown in Fig. 7a. Enhanced NO_2 density is observed along the major shipping lane over the BoB compared to the surrounding oceanic regions, indicating that NO_2 density can be safely used to represent shipping activities. Note that the enhanced NO_2 density could also be partially attributed to the enhanced lightning, given that lightning can produce nitric oxide (NO) that can be further oxidized into NO_2[38,39]. While NO_2 density showed positive changes over the South China Sea from 2019 to the post-regulation period (2020–2023), no spatially homogeneous changes were observed over the BoB. Therefore, we argue that i) the enhanced NO_2 is dominated by direct shipping emissions rather than enhanced lightning-produced NO_2; and more importantly, ii) the direct ship interactions alone can hardly explain the lightning enhancement; and in addition, iii) the 36% reduction in the lightning density during the post-regulation period can be attributed to both the IMO 2020 regulation and changes in the meteorological conditions because shipping activities showed little changes after 2020.

The contribution of the changes in meteorological conditions to the reduced lightning density after 2020 within the shipping lane area can be estimated using the counterfactual values in Fig. 2d, f as −0.24 (0.57 minus 0.81) strokes km^{-2} $year^{-1}$ (−24%). Then the contribution of the shipping emissions is −0.11 (−0.35 in total variations minus −0.24) strokes km^{-2} $year^{-1}$ (−11%). Ideally, the counterfactual values should represent the impacts of meteorological conditions alone. However, because small but nonzero shipping emissions are present in the reference lanes, the counterfactual values contain the impacts of both meteorological conditions and shipping emissions on the lightning density. Therefore, the estimated impact of the meteorological conditions here represents its upper bound value, yet the estimated impact of the shipping emissions represents its lower bound value.

The Community Emissions Data System (CEDS) demonstrates that SO_2 emissions from international shipping over the shipping lane in the BoB decreased by 66% from the period of 2012–2019 to 2020–2022. By assuming a linear relationship between SO_2 emissions and lightning density, a zero SO_2 emission from shipping would result in a reduction of at least 17% (11%/66%) in lightning density.

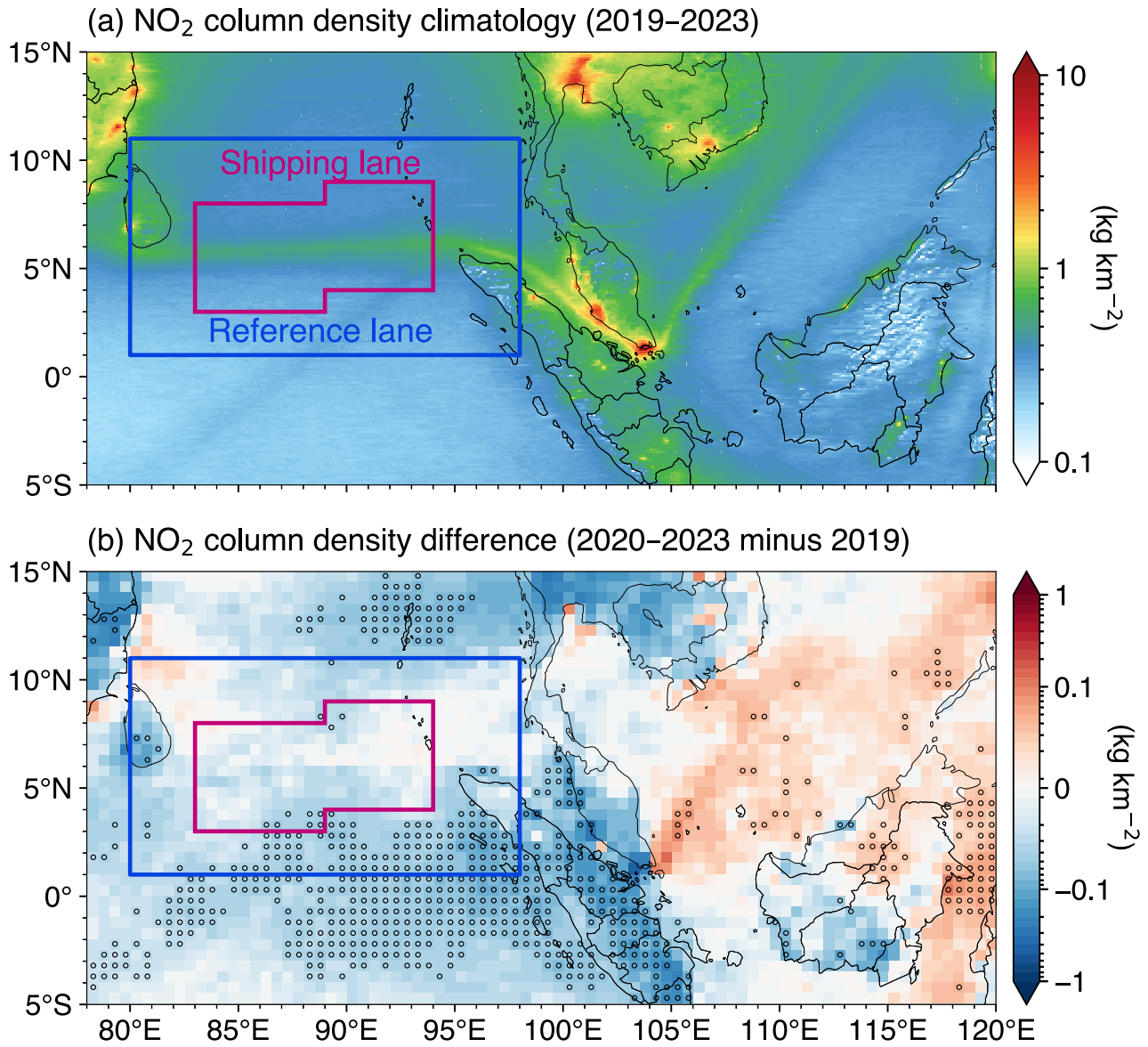

Fig. 7 | Nitrogen dioxide (NO_2) column density in the troposphere. a Climatology (2019–2023) and **b** differences (2020–2023 mean minus 2019) of NO_2 column density (kg m^{-2}) in the troposphere. Circles in panel **b** indicate grid cells with statistically significant differences at 95% confidence level. Data are from TROPOMI. The figure was created using Matplotlib Python package.

Discussion

In this study, we use data from a global lightning location network and satellite-retrieved cloud products to investigate the physical mechanisms behind frequent lightning activity along the major shipping lane over the Bay of Bengal (BoB). Additionally, we examine the reduction in lightning density and changes in cloud properties resulting from the IMO 2020 regulation. Our findings show that the enhanced lightning density along the shipping lane, centered at ~5.5°N, compared to surrounding regions, is closely linked to changes in cloud properties, including higher tops of mid-to-high clouds, smaller cloud droplets in low clouds, greater ice water paths between 3 and 15 km, and smaller ice particles between 4 and 20 km. These changes in cloud properties are attributed to sulfate aerosols from shipping emissions. Further analysis reveals that the contrasts in all these cloud properties except ice particle radius between the shipping lane vs. surrounding regions have significantly decreased after the implementation of stricter sulfur emissions regulations by the IMO in 2020. Given that satellite data shows no significant change in shipping activity, we conclude that the reduction in shipping emissions is the main driver of the 11% decline in lightning activity since 2020. The interactions between ship-derived sulfate aerosols and clouds likely play a more important role than direct shipping interactions in this reduction in lightning occurrence. Our results provide robust observational evidence of the impact of anthropogenic sulfate aerosols on deep convection by modulating both micro- and macro-properties of clouds. More specifically, reduced sulfate aerosols can result in less but larger cloud droplets, which could cause stronger downdraft and thus weaken the updraft in a thunderstorm, consistent with the observed lower cloud top. A lower cloud top could constrain the supercooled water at a relatively warm temperature, which in combination with less INP due to reduced sulfate aerosols can reduce the production of ice crystals through the heterogeneous ice nucleation process, as indicated by observed less ice water path. A less ice water path implies less latent heat released within the thunderstorm which can inhibit further development of the thunderstorm into a higher altitude, forming a positive feedback loop. The above discussed changes in shallow and deep cloud properties initialized by the ship-induced reduction in sulfate aerosols could ultimately reduce the rebounding collisions between graupels and ice crystals, charge separation, and lightning activities.

Three key caveats should be considered in this study. First, the assumed linear relationship between the reductions in sulfur emissions due to the shipping regulations and changes in lightning density may introduce uncertainties, particularly when estimating the relative importance of aerosol–cloud interactions versus direct shipping interactions on lightning enhancement over the BoB. Future studies should address this uncertainty by using numerical models that well capture the non-linearity in aerosol–cloud interactions[24,40]. This uncertainty may also be addressed based on future observations if the IMO implements even stricter sulfur content regulations (e.g., reducing sulfur from 0.5% to 0.1%). The second caveat concerns the counterfactual values derived using the kriging method. While these values help isolate the impacts of shipping emissions, they may still underestimate their full effects on clouds and lightning. Quantifying the extent to which this underestimation could bias the attribution of the lightning changes to the shipping emission regulation is challenging based on observations but could be well addressed through model simulations in future research. The third caveat relates to the seasonality of lightning activities and its decline since 2020. Preliminary analysis (Supplementary Fig. S6) shows more frequent lightning and greater declines during convectively active seasons (boreal winter and spring) compared to other seasons. This study focuses on annual rather than seasonal changes due to the limited data (only four years since 2020), which makes robust statistical analysis of seasonal changes challenging. As the first attempt to demonstrate the statistical robustness of the lightning density changes during the climatology and post-regulation periods, we calculated standard errors of the monthly means based on the interannual variability. As shown in Supplementary Fig. S6, no overlap was seen between the monthly mean lightning densities ± one standard error during the two periods in all months except for July, August, and March, indicating the monthly changes are robust based on the applied statistical method. The annual means of lightning densities are 0.98 ± 0.06 vs. 0.63 ± 0.03 (one standard error) strokes km^{-2} yr^{-1} for the climatology and post-regulation periods, respectively. The two numbers are far part by more than 3 standard errors, indicating the decrease in annual lightning density is very robust. As more data becomes available, more sophisticated and powerful statistical methods can be used to estimate the confidence intervals of the changes in the lightning activities.

Previous studies have highlighted that the enhanced lightning activity along the shipping lane, compared to surrounding regions, is most evident over the BoB and South China Sea[17,20]. However, a question remains: Why is lightning enhancement not observed over other busy shipping lanes, such as the Gulf of Mexico, which are far from continental influence and possess convective environment? One possible reason is that ship-derived sulfate aerosols may not lead to a significant increase in ice cloud particles along these shipping lanes, possibly due to differences in atmospheric dynamics or thermodynamical conditions. Future research contrasting environments over shipping lanes with versus without lightning enhancement could provide insights into aerosol activation conditions in deep convective storms, where observing cloud properties remains challenging from both satellites and aircraft.

Although this study focuses on a regional domain, its findings have significant implications for the global climate. As more countries implement stricter air pollution standards to improve air quality, sulfate aerosols and other hygroscopic aerosol species–key CCN and INP–are showing decreasing trends across continents, particularly in North America, Europe, and East Asia[4,41]. The decline in these aerosol concentrations may reduce lightning activities on a global scale, potentially leading to fewer lightning-ignited wildfires[42–44] and a decrease in lightning-produced nitrogen oxides[39,45], which could disrupt Earth's biogeochemical cycles. Moreover, a better understanding of meteorological conditions for aerosol activation could reduce uncertainties in the estimates of global aerosol forcing and climate sensitivity, ultimately improving the accuracy of future climate projections.

Methods

WWLLN

(The World Wide Lightning Location Network) observes global lightning strokes from 2004 to the present[46]. WWLLN operates over 70 sensors around the world, each of which monitors very low-frequency radiation and detects lightning strokes[47]. Each lightning stroke is recorded with latitude, longitude, and time stamp when at least five sensors detect the stroke. The location and time accuracy are 3.4 km and 1 microsecond, respectively[48]. In this study, the raw data are re-gridded into a regular latitude-longitude grid map of 1° × 1°. The annual lightning density is calculated by aggregating the counts of lightning strokes within each grid cell over a year and then dividing the total number of lightning strokes by the area of each grid cell, resulting in a unit of strokes km^{-2} $year^{-1}$. Here, only data from 2012 to 2023 are used because the number of sensors has continued to increase before 2012[49], which could introduce uncertainty in our analysis and thus be neglected.

CEDS

(The Community Emissions Data System) estimates anthropogenic emissions by country, sector, and fuel[9,50]. The emissions are estimated based on 1) energy production and consumption data compiled by the International Energy Agency, 2) population data from the United Nations and World Bank, and 3) emission factors for combustion and non-combustion emissions. The data have an annual temporal resolution and two spatial resolutions at 0.5° × 0.5° and 0.1° × 0.1°, covering a period from 1750 to 2022. The data are interpolated to 1° resolution to keep consistency with other datasets. Here, SO_2 emissions from the sector of international shipping (1A3di-International-shipping) are used to find the shipping lanes over the Bay of Bengal. The data are available at https://github.com/JGCRI/CEDS.

CERES

(The Clouds and the Earth's Radiant Energy System) instrument onboard the Terra satellite measures the Earth's energy budget and cloud properties[51]. Cloud properties are extracted from the level 3 gridded 1° × 1° monthly averages of the Single Scanner Footprint product (SSF1deg)[52]. These properties include cloud top height for mid-to-high clouds and water particle radius at 3.7 μm for low clouds. The low and mid-to-high clouds are defined as clouds between surface and 700 hPa (~3 km) and between 500 hPa (~5 km) and 300 hPa (~9 km), respectively. The monthly data from January 2012 to December 2023 are used.

CALIOP

(The Cloud-Aerosol Lidar with Orthogonal Polarization) instrument onboard the Cloud-Aerosol Lidar and Infrared Pathfinder Satellite Observations (CALIPSO) satellite is used to obtain the vertical profiles of ice cloud microphysical properties[53,54]. The properties of the ice cloud are derived from the extinction profiles of the clouds at 532 nm. Here, the level 2 cloud profile product (CAL_LID_L2_05kmCPro-Standard-V4-51) of ice water content was analyzed. The cloud profiles have 399 layers that extend from the surface to an altitude of 29.8 km, with vertical resolutions of 60 and 180 m below and above 20.2 km, respectively, and a horizontal resolution of 5 km. In total, there are 488,349 profiles selected within a rectangular area of 1–11 °N and 80–98 °E from June 2006 to June 2023. The spatial distribution of these profiles is shown in Supplementary Fig. S7.

2C-ICE

(The CloudSat and CALIPSO Ice Cloud Property Product) provides profiles of effective radius and other properties of ice clouds. The 2C-ICE product was produced by combing the measured radar reflectivity factor by CloudSat and measured attenuated backscattering coefficients at 532 nm by CALIOP to reduce the biases of ice cloud retrieval[55,56]. The profiles have 125 layers that extend from the surface to 24.9 km, with a vertical and horizontal resolutions of 240 m and 1.1 km, respectively. There is a total of 1,184,075 profiles within the area of 1–11 °N and 80–98 °E from June 2006 to December 2019. Note that following the re-gridding method used in the WWLLN dataset, both the profiles of CALIOP and 2C-ICE are re-gridded

into a regular latitude-longitude grid map of 1° × 1° to keep consistency with CERES data resolution.

ERA5

(The European Centre for Medium-Range Weather Forecasts (ECMWF) Reanalysis v5) is the atmospheric reanalysis of global climate[57]. It has a spatial resolution of 31 km, covering a period from January 1940 to present. Here, monthly horizontal wind fields at 850 hPa from 1940 to 2023 are averaged to achieve the climatology.

TROPOMI

(The TROPOspheric Monitoring Instrument) onboard the European Space Agency Copernicus Sentinel-5 Precursor satellite monitors trace gases and aerosols for air quality and climate research[58]. It is a low Earth orbit polar satellite with a swath width of 2600 km, which makes it have a daily near-global coverage. Based on radiance measured in the ultraviolet-visible-near infrared-shortwave infrared spectrum, TROPOMI retrieves aerosol properties and atmospheric densities of trace gases including NO_2, SO_2, O_3, CO, CH_4, and CH_2O with a spatial resolution of 5.5 km × 3.5 km. Here, NO_2 and SO_2 data of version 2 from 2019 to 2023 are used. NO_2 and SO_2 retrievals are based on the radiance in the visible (400–496 nm) and ultraviolet–visible channels, respectively[59–62]. Not that the retrieval accuracy of SO_2 concentration in the troposphere from space is intrinsically limited by the Rayleigh and Mie scattering and ozone absorption of ultraviolet radiation, which hampers the penetration of ultraviolet radiation to the lowest atmospheric layer[59]. Consequently, SO_2 concentration does not show a clear footprint along major shipping lanes, as shown in Supplementary Fig. S8.

Identification of shipping and reference lanes

The shipping lane is identified based on CEDS SO_2 emissions of one-degree spatial resolution following the method of Diamond[23]. For each longitude between 82 °E and 94 °E, the shipping lane grid cells are identified as those with annual maximum SO_2 emission rates between 1 °N and 11 °N as well as two grid cells to the south and two to the north. This results in 55 shipping lane grid cells as shown in Fig. 1, with the coordinates of 11 grid cells at the center of the ship lanes (longitude: increasing from 83.5 to 93.5 °E by every degree; latitude: 5.5, 5.5, 5.5, 5.5, 5.5, 5.5, 6.5, 6.5, 6.5, 6.5, and 6.5 °N). The reference lane grid cells are defined as those within a box area of 80–98 °E and 1–11 °N excluding the shipping lane grid cells. The strong seasonality of wind direction (i.e., from northerly to southerly shifts in winter and summer) over the Bay of Bengal can disperse the shipping emissions to the adjacent regions of the east-west oriented ship track. Therefore, including two degrees to the south and two degrees to the north in the definition of the shipping lane can largely reduce the impacts of emission dispersion on the robustness of the Kriging method.

Regression kriging

Kriging is a geostatistical interpolation algorithm to estimate a field at locations without observations by using nearby observations based on the assumed spatial covariance in the field[63]. Regression kriging is employed here that combines regression of the dependent variable in auxiliary information with interpolation of the residuals of the regression model[64]. Unlike universal kriging, which directly uses the auxiliary information to solve kriging weights, regression kriging explicitly separates trend/drift estimation from the residual interpolation, allowing the use of complex regression models rather than the simple linear regression method. Using the method similar to Diamond[23], the random forest regression model is selected as the mean function with regressors taking the form of various combinations of SSF1deg auxiliary data (i.e., surface skin temperature (SST), wind speed (WS), estimated inversion strength (EIS)) and coordinate data (i.e., longitude (lon), latitude (lat), lon^2, lat^2, and product of lat and lon), as determined by the combination that maximizes the coefficient of determination associated with the regression model.

In this study, the effects of shipping activity on lightning density and cloud properties are quantified by examining the difference between the factual (observed) and counterfactual values of cloud micro- and macrophysical properties. The counterfactual values are estimated in the absence of shipping activity by applying the regression kriging method. First, the random forest regression model is fitted based on the SSF1deg auxiliary data and coordinate data in the grid cells within the reference lane. Second the fitted regression model is used to predict the counterfactual values using the data in the grid cells within the shipping lane. The factual (observed) and counterfactual values of a variable, X, are referred to as "X_{Ship}" and "X_{NoShip}", respectively; the difference is denoted as $\Delta X_{\mathrm{Ship-NoShip}}$ and attributed to the presence of shipping activity. Note that the kriging method is not perfect, because the counterfactual values cannot completely rule out the impacts of shipping emissions. This imperfection would cause underestimations of the impacts of the shipping emissions on the lightning frequency and cloud properties. The kriging analysis is performed by using the kriging toolkit for Python—PyKrige (https://geostat-framework.readthedocs.io/projects/pykrige/en/stable/).

Statistically significant testing

Two-tailed 95% confidence intervals and p-value are used in this study to assess the statistical significance of the differences between factual and the counterfactual values derived from the kriging method. The two parameters are calculated through the nonparametric bootstrap hypothesis. The confidence intervals are calculated as the 2.5th and 97.5th percentiles of the distribution of the differences that are produced by resampling the differences with replacement by 10,000 times. Statistical significance for each shipping lane grid cell is evaluated as whether the 95% confidence intervals of the difference between the observed and counterfactual values encompasses zero. The p-value associated with the difference is estimated in the following 5 steps: 1) calculate the absolute value of the difference between the means of m observational values and n counterfactual values; 2) randomly select t ($t = m + n$) values from the combined observational and counterfactual values; 3) calculate the absolute value of the difference between the means of the first m and last n values in the randomly select values in step 2); 4) repeat steps 2) and 3) for 10,000 times and count the number of the occurrence where the absolute value of the difference in step 3) is greater than that in step 1); 5) the p-value is estimated as the ratio of the count in step 4) to 10,000. Note that the mean of the absolute values of the difference in step 3 should be close to zero because the two groups of values are randomly selected from the same data series.

Data availability

All data and materials used in the analyses are freely available. The information of the WWLLN data can be found at https://wwlln.net/ and downloaded at https://zenodo.org/records/10725446. The CEDS data are available at https://github.com/JGCRI/CEDS/. The satellite datasets and their download links are listed here: CERES (https://ceres.larc.nasa.gov/data/), CALIPSO (https://asdc.larc.nasa.gov/), 2C-ICE (https://www.cloudsat.cira.colostate.edu/), and TROPOMI (https://disc.gsfc.nasa.gov/). The ERA5 data can be found at https://doi.org/10.24381/cds.6860a573.

Code availability

The underlying code for this study is not publicly available but may be made available to qualified researchers on reasonable request from the corresponding author.

Received: 4 July 2025; Accepted: 4 October 2025;
Published online: 04 November 2025

References

1. Szopa, S. et al. Short-Lived Climate Forcers. In *Climate Change 2021: The Physical Science Basis. Contribution of Working Group I to the Sixth Assessment Report of the Intergovernmental Panel on Climate Change*, Masson-Delmotte, V. et al. (eds), pp. 817–922 (Cambridge University Press, Cambridge, United Kingdom and New York, NY, USA, 2021). https://doi.org/10.1017/9781009157896.008.

2. Twomey, S. Pollution and the planetary albedo. *Atmos. Environ.* **8**, 1251–1256 (1974).
3. Forster, P. M. et al. The Earth's energy budget, climate feedbacks and climate sensitivity. In *Climate Change 2021 – The Physical Science Basis*, 923–1054 (IPCC, 2023).
4. Quaas, J. et al. Robust evidence for reversal of the trend in aerosol effective climate forcing. *Atmos. Chem. Phys.* **22**, 12221–12239 (2022).
5. Gettelman, A. et al. Has reducing ship emissions brought forward global warming?. *Geophys. Res. Lett.* **51**, e2024GL109077 (2024).
6. Jordan, G. & Henry, M. IMO2020 regulations accelerate global warming by up to 3 years in UKESM1. *Earth Fut.* **12**, e2024EF005011 (2024).
7. Hansen, J. E. et al. Global warming has accelerated: are the United Nations and the public well-informed?. *Environ. Sci. Policy Sustain. Dev.* **67**, 6–44 (2025).
8. Hansen, J. E. et al. Global warming in the pipeline. *Oxford Open Clim. Change* **3**, kgad008 (2023).
9. McDuffie, E. E. et al. A global anthropogenic emission inventory of atmospheric pollutants from sector-and fuel-specific sources (1970–2017): an application of the Community Emissions Data System (CEDS). *Earth Syst. Sci. Data* **12**, 3413–3442 (2020).
10. Christensen, M. W. et al. Opportunistic experiments to constrain aerosol effective radiative forcing. *Atmos. Chem. Phys.* **22**, 641–674 (2022).
11. Conover, J. H. Anomalous cloud lines. *J. Atmos. Sci.* **23**, 778–785 (1966).
12. Christensen, M. W. & Stephens, G. L. Microphysical and macrophysical responses of marine stratocumulus polluted by underlying ships: evidence of cloud deepening. *J. Geophys. Res.* **116**, D03201 (2011).
13. Glassmeier, F. et al. Aerosol-cloud-climate cooling overestimated by ship-track data. *Science* **371**, 485–489 (2021).
14. Watson-Parris, D. et al. Shipping regulations lead to large reduction in cloud perturbations. *Proc. Natl. Acad. Sci.* **119**, e2206885119 (2022).
15. Twomey, S., Howell, H. & Wojciechowski, T. Comments on "anomalous cloud lines. *J. Atmos. Sci.* **25**, 333–334 (1968).
16. Blossey, P. N. et al. Locally enhanced aerosols over a shipping lane produce convective invigoration but weak overall indirect effects in cloud-resolving simulations. *Geophys. Res. Lett.* **45**, 9305–9313 (2018).
17. Thornton, J. A. et al. Lightning enhancement over major oceanic shipping lanes. *Geophys. Res. Lett.* **44**, 9102–9111 (2017).
18. Sun, R. et al. The impacts of shipping emissions on lightning: roles of aerosol-radiation-interactions and aerosol-cloud-interactions. *Environ. Res. Lett.* **19**, 034038 (2024).
19. Qie, X. et al. Lightning response to temperature and aerosols. *Environ. Res. Lett.* **19**, 083003 (2024).
20. Peterson, M. Interactions between lightning and ship traffic. *Earth Space Sci.* **10**, e2023EA002926 (2023).
21. Forster, P. M. et al. Indicators of Global Climate Change 2023: annual update of key indicators of the state of the climate system and human influence. *Earth Syst. Sci. Data* **16**, 2625–2658 (2024).
22. Yuan, T. et al. Global reduction in ship-tracks from sulfur regulations for shipping fuel. *Sci. Adv.* **8**, eabn7988 (2022).
23. Diamond, M. S. Detection of large-scale cloud microphysical changes within a major shipping corridor after implementation of the International Maritime Organization 2020 fuel sulfur regulations. *Atmos. Chem. Phys.* **23**, 8259–8269 (2023).
24. Jin, Q. et al. Impacts on cloud radiative effects induced by coexisting aerosols converted from international shipping and maritime DMS emissions. *Atmos. Chem. Phys.* **18**, 16793–16808 (2018).
25. Wright, C. J. et al. Lightning declines over shipping lanes following regulation of fuel sulfur emissions. *Atmos. Chem. Phys.* **25**, 2937–2946 (2025).
26. Vongpaseut, I. & Barthe, C. Distinct effects of several ice production processes on thunderstorm electrification and lightning activity. *EGUsphere* **2025**, 1–34 (2025).
27. Saunders, C. Charge separation mechanisms in clouds. *Space Sci. Rev.* **137**, 335–353 (2008).
28. Lopez, P. A lightning parameterization for the ECMWF integrated forecasting system. *Monthly Weather Rev.* **144**, 3057–3075 (2016).
29. Finney, D. L. et al. A projected decrease in lightning under climate change. *Nat. Clim. Change* **8**, 210–213 (2018).
30. Jacobson, M. Z. & Streets, D. G. Influence of future anthropogenic emissions on climate, natural emissions, and air quality. *J. Geophys. Res.* **114**, D08118 (2009).
31. Tang, M., Cziczo, D. J. & Grassian, V. H. Interactions of water with mineral dust aerosol: water adsorption, hygroscopicity, cloud condensation, and ice nucleation. *Chem. Rev.* **116**, 4205–4259 (2016).
32. Kanji, Z. A. et al. Overview of ice nucleating particles. *Meteorol. Monogr.* **58**, 1.1–1.33 (2017).
33. Kumar, V. V. et al. On the atmospheric regulation of the growth of moderate to deep cumulonimbus in a tropical environment. *J. Atmos. Sci.* **71**, 1105–1120 (2014).
34. Dong, X. et al. Comparison of CERES-MODIS stratus cloud properties with ground-based measurements at the DOE ARM Southern Great Plains site. *J. Geophys. Res.* **113**, D03204 (2008).
35. Christensen, M. W., Jones, W. K. & Stier, P. Aerosols enhance cloud lifetime and brightness along the stratus-to-cumulus transition. *Proc. Natl. Acad. Sci.* **117**, 17591–17598 (2020).
36. Koren, I. et al. Aerosol invigoration and restructuring of Atlantic convective clouds. *Geophys. Res. Lett.* **32**, L14828 (2005).
37. Cui, Z. et al. The response of precipitation to aerosol through riming and melting in deep convective clouds. *Atmos. Chem. Phys.* **11**, 3495–3510 (2011).
38. Wang, C. & Prinn, R. G. On the roles of deep convective clouds in tropospheric chemistry. *J. Geophys. Res.* **105**, 22269–22297 (2000).
39. Pérez-Invernón, F. J. et al. Lightning-produced nitrogen oxides per flash length obtained by using TROPOMI observations and the Ebro lightning mapping array. *Geophys. Res. Lett.* **50**, e2023GL104699 (2023).
40. Thomas, M. A. et al. Rate of non-linearity in DMS aerosol-cloud-climate interactions. *Atmos. Chem. Phys.* **11**, 11175–11183 (2011).
41. Hu, Z. et al. Temporal evolution of aerosols and their extreme events in polluted Asian regions during Terra's 20-year observations. *Remote Sens. Environ.* **263**, 112541 (2021).
42. Schultz, C. J. et al. Spatial, temporal, and electrical characteristics of lightning in reported lightning-initiated wildfire events. *Fire* **2**, 2020018 (2019).
43. Song, Y. et al. Lightning-induced wildfires: an overview. *Fire* **7**, 79 (2024).
44. Krause, A. et al. The sensitivity of global wildfires to simulated past, present, and future lightning frequency. *J. Geophys. Res.* **119**, 312–322 (2014).
45. Zhang, X. et al. Estimates of lightning NOx production based on high-resolution OMI NO_2 retrievals over the continental US. *Atmos. Meas. Tech.* **13**, 1709–1734 (2020).
46. Virts, K. S. et al. Highlights of a new ground-based, hourly global lightning climatology. *Bull. Am. Meteorol. Soc.* **94**, 1381–1391 (2013).
47. Dowden, R. L., Brundell, J. B. & Rodger, C. J. VLF lightning location by time of group arrival (TOGA) at multiple sites. *J. Atmos. Sol. Terrestrial Phys.* **64**, 817–830 (2002).
48. Rodger, C., Brundell, J, & Dowden, R. Location accuracy of VLF World-Wide Lightning Location (WWLL) network: post-algorithm upgrade. In *Annales Geophysicae* (Copernicus Publications Göttingen, 2005).
49. Kaplan, J. O. & Lau, K. H.-K. World wide lightning location network (WWLLN) global lightning climatology (WGLC) and time series, 2022 update. *Earth Syst. Sci. Data* **14**, 5665–5670 (2022).

50. Hoesly, R. M. et al. Historical (1750–2014) anthropogenic emissions of reactive gases and aerosols from the Community Emissions Data System (CEDS). *Geosci. Model Dev.* **11**, 369–408 (2018).
51. Loeb, N. et al. Earth's top-of-atmosphere radiation budget. *Compr. Remote Sens.* **5**, 67–84 (2018).
52. Yost, C. R. et al. CERES MODIS cloud product retrievals for edition 4—Part II: comparisons to CloudSat and CALIPSO. *IEEE Trans. Geosci. Remote Sens.* **59**, 3695–3724 (2020).
53. Avery, M. et al. Cloud ice water content retrieved from the CALIOP space-based lidar. *Geophys. Res. Lett.* **39**, L05808 (2012).
54. Winker, D. et al. The CALIPSO mission: A global 3D view of aerosols and clouds. *Bull. Am. Meteorol. Soc.* **91**, 1211–1230 (2010).
55. Deng, M. et al. CloudSat 2C-ICE product update with a new Ze parameterization in lidar-only region. *J. Geophys. Res. Atmos.* **120**, 12198–12208 (2015).
56. Stephens, G. L. et al. The CloudSat mission and the A-Train: a new dimension of space-based observations of clouds and precipitation. *Bull. Am. Meteorol. Soc.* **83**, 1771–1790 (2002).
57. Hersbach, H. et al. The ERA5 global reanalysis. *Q. J. R. Meteorol. Soc.* **146**, 1999–2049 (2020).
58. Veefkind, J. P. et al. TROPOMI on the ESA Sentinel-5 Precursor: a GMES mission for global observations of the atmospheric composition for climate, air quality and ozone layer applications. *Remote Sens. Environ.* **120**, 70–83 (2012).
59. Theys, N. et al. Sulfur dioxide retrievals from TROPOMI onboard Sentinel-5 Precursor: algorithm theoretical basis. *Atmos. Meas. Tech.* **10**, 119–153 (2017).
60. van Geffen, J. et al. S5P TROPOMI NO_2 slant column retrieval: method, stability, uncertainties and comparisons with OMI. *Atmos. Meas. Tech.* **13**, 1315–1335 (2020).
61. van Geffen, J. et al. Sentinel-5P TROPOMI NO_2 retrieval: impact of version v2.2 improvements and comparisons with OMI and ground-based data. *Atmos. Meas. Tech.* **15**, 2037–2060 (2022).
62. Theys, N. et al. A sulfur dioxide Covariance-Based Retrieval Algorithm (COBRA): application to TROPOMI reveals new emission sources. *Atmos. Chem. Phys.* **21**, 16727–16744 (2021).
63. Gelfand, A. E. et al. *Handbook of Spatial Statistics* (CRC press, 2010).
64. Hengl, T., Heuvelink, G. B. & Rossiter, D. G. About regression-kriging: from equations to case studies. *Comput. Geosci.* **33**, 1301–1315 (2007).

Acknowledgements

We thank Dr. Chien Wang for his valuable comments on the early versions of this paper. The authors wish to thank the World Wide Lightning Location Network (http://wwlln.net), a collaboration among over 50 universities and institutions, for providing the lightning location data used in this paper. No funding was received for conducting this study.

Author contributions

Conceptualization: Q.J. and B.P. Methodology: Q.J. Formal analysis: Q.J. Investigation: Q.J. Visualization: Q.J. Writing—original draft: Q.J. Writing—review & editing: Q.J., B.P., J.H., and J.W.

Competing interests

The authors declare no competing interests.

Additional information

Supplementary information The online version contains supplementary material available at https://doi.org/10.1038/s41612-025-01256-w.

Correspondence and requests for materials should be addressed to Qinjian Jin or Bing Pu.